Research
A SCIENCE PARTNER JOURNAL

RESEARCH ARTICLE

Photo-Responsive Carbon Capture over Metalloporphyrin-C_{60} Metal-Organic Frameworks via Charge-Transfer

Shi-Chao Qi, Zhen Sun, Zhi-Hui Yang, Yun-Jie Zhao, Jia-Xin Li, Xiao-Qin Liu, and Lin-Bing Sun*

State Key Laboratory of Materials-Oriented Chemical Engineering, Jiangsu National Synergetic Innovation Center for Advanced Materials (SICAM), College of Chemical Engineering, Nanjing Tech University, Nanjing 211816, China.

*Address correspondence to: lbsun@njtech.edu.cn

Citation: Qi SC, Sun Z, Yang ZH, Zhao YJ, Li JX, Liu XQ, Sun LB. Photo-Responsive Carbon Capture over Metalloporphyrin-C_{60} Metal-Organic Frameworks via Charge-Transfer. *Research* 2023;6:Article 0261. https://doi.org/10.34133/research.0261

Submitted 14 August 2023
Accepted 10 October 2023
Published 24 October 2023

Copyright © 2023 Shi-Chao Qi et al. Exclusive licensee Science and Technology Review Publishing House. No claim to original U.S. Government Works. Distributed under a Creative Commons Attribution License 4.0 (CC BY 4.0).

Great efforts have been devoted to the study of photo-responsive adsorption, but its current methodology largely depends on the well-defined photochromic units and their photo-driven molecular deformation. Here, a methodology to fabricate nondeforming photo-responsive sorbents is successfully exploited. With C_{60}-fullerene doping in metalloporphyrin metal-organic frameworks (PCN-M, M = Fe, Co, or Ni) and intensively interacting with the metalloporphyrin sites, effective charge-transfer can be achieved over the metalloporphyrin-C_{60} architectures once excited by the light at 350 to 780 nm. The electron density distribution and the resultant adsorption activity are thus changed by excited states, which are also stable enough to meet the timescale of microscopic adsorption equilibrium. The charge-transfer over Co(II)-porphyrin-C_{60} is proved to be more efficient than the Fe(II)- and Ni(II)-porphyrin-C_{60} sites, as well as than all the metalloporphyrin sites, so the CO_2 adsorption capacity (CAC; at 0 °C and 1 bar) over the C_{60}-doped PCN-Co can be largely improved from 2.05 mmol g^{-1} in the darkness to 2.69 mmol g^{-1} with light, increased by 31%, in contrast to photo-irresponsive CAC over all C_{60}-undoped PCN-M sorbents and only the photo-loss CAC over C_{60}.

Introduction

Traditional technologies of adsorption separation such as pressure swing adsorption, temperature swing adsorption, and vacuum swing adsorption always require large power quantities [1–4]. Stimuli-responsive adsorption separation is promising to provide high adsorption capability and selectivity but without additional power burden, such as guest-molecular and temperature-responsive adsorption [5–7]. In view of the great market prospect of solar energy, how to introduce optical factors in the adsorption separation are attractive, and thus, great efforts have been devoted to the study of photo-responsive or photo-stimuli sorbents [8–11]. Majority of current photo-responsive sorbents are designed to exploit the deformation of photochromic units [12–14], such as azobenzenes, diarylethenes, and spiropyrans, which are treated as the guest molecules to be integrated within the host materials like metal-organic frameworks (MOFs), covalent-organic frameworks (COFs), and mesoporous zeolites [15–17]. Once the photochromic units deformed owing to photo-stimulation, e.g., the trans-to-cis azobenzene and the open-to-close diarylethene ring with the ultraviolet (UV) irradiation, the steric effect or the polarity nearby the adsorption sites can be changed, resulting in the photo-modulated adsorption capability of the host material [18–22]. However, in most cases, the photo-responsive sorbents so prepared only exhibit the adsorption capability decrease with light, owing to the limitations of the deforming mechanism.

The photo-modulated adsorption capability does not perforce depending on the deformation of photochromic units when we realize that the specific adsorption capability exhibited by an adsorption site is ultimately attributed to its specific electron density distribution (EDD), which is invariable only at ground states, namely, Hohenberg–Kohn theorem [23]. Once the adsorption site is excited by photo-stimulation, the EDD can be evolved, and thus, the modulated adsorption capability can be expected even without molecular deformation [24,25]. Anyway, it is difficult to dramatically alter the EDD because the electron hole is largely overlapped for the local excitation with long lifetimes, whereas a charge-transfer (CT) excitation that can effectively alter the EDD is easily quenched, which cannot meet the timescale of microscopic adsorption equilibrium. The areas of artificial photosynthesis and organic photovoltaics related to light harvest and conversion afforded us experiences [26–28]. In these areas, the electron donor–acceptor systems were fabricated to attain long-lived CT states. In particular, fullerenes, as efficient π-electron acceptors due to highly delocalized π-electrons over the 3-dimensional π-sphere, can be coupled with porphyrins as the electron donors to form diverse dyads with efficient CT and energy-transfer processes [29]. For example, the CT state that resulted from the excitation of a triad,

constructed by linking C_{60} and bis(3,4,5-trimethoxyphenyl) aniline to Al(III)-porphyrin, lies energetically 1.50 eV above the ground state [30].

In this research, we expand the methodology of photoinduced CT state to the photo-responsive adsorption separation for the first time. Without photochromic units deforming, the methodology of nondeforming photo-responsiveness to efficiently modulate the EDD of adsorption sites is realized through photoinduced CT. We employed the metalloporphyrin MOF of PCN-222-M [PCN-M for short, and M = Fe(II), Co(II), or Ni(II)] and the fullerene of C_{60} to fabricate corresponding composite material, code-named CPCN-M, which are then used as the sorbents for the photoinduced selective adsorption of CO_2 (Fig. 1). As a promising approach for carbon capture, adsorption separation has drawn much attention [31,32]. In particular, the direct air capture (DAC) as the new generation of carbon capture technology may have to mimic the biological photosynthetic carbon sequestration [33,34]. For example, microalgae cultures have promise as a CO_2 sink for atmospheric carbon and as a sustainable source of food and chemical feedstocks [35]. Therefore, a sorbent that can exhibit enhanced CO_2 adsorption capability in the sunlight sounds inspiring. Here, all the C_{60}-undoped PCN-Ms do not exhibit noticeable changes of CO_2 adsorption capability with UV-visible (UV-Vis) irradiation; meanwhile, the CO_2 uptake capacity over C_{60} only decreases with the UV-Vis irradiation. In contrast, their composite sorbents CPCN-Ms exhibit marked photo-responsiveness in terms of CO_2 adsorption capability. For instance, the CO_2 adsorption capacity (0 °C, 1 bar) of CPCN-Co is elevated from 2.05 mmol g^{-1} in the darkness to 2.69 mmol g^{-1} with the UV-Vis irradiation, increased by 31%. Moreover, even though the porphyrin-coordinated metals in CPCN-Ms, i.e., Fe, Co, and Ni, only differ by an electron, we prove that their CT modes and resultant macroscopical adsorption performances with the UV-Vis are totally different from each other.

Results

Materials characteristics

Unless otherwise noted, the mass ratio between C_{60} and PCN-M for CPCN-M is 1:8, which exhibits better adsorption capability and more obvious photo-responsiveness than those with other mass ratios, as discussed in the following section. The crystalline grains of as-prepared CPCN-Ms are neat and uniform, and introducing C_{60} does not influence the successful crystallization (Fig. S1). It can be further confirmed through x-ray powder diffraction (XRPD). The XRPD patterns of CPCN-Ms, which are also not changed by the type of the porphyrin-coordinated metal, are consistent with that of PCN-M reported (Fig. S2) [36–38]. The successful preparation of CPCN-Ms can be proved by the Fourier transform infrared (FTIR) spectra. The characteristic band of C_{60} at 1180 cm^{-1} is retained for the FTIR spectra of CPCN-Ms, in which the characteristic bands located at 1006 cm^{-1} indicate that the presence of porphin-*N*-metal bonds can also be seen (Fig. S3). In the high-resolution electron microscopy (HREM) images (Fig. S4), the structured C_{60} aggregation attached to the MOF grain crystals can be seen occasionally, and a considerable number of C_{60} molecules ought to be monodispersed among the crystal lattices of the MOFs, manifested as bright spots with the size of 0.7 nm at the accelerating voltage of 200 kV [39,40]. Moreover, owing to the doped C_{60} molecules, the observed lattice distance (ca. 2.6 nm) of CPCN-M is stretched compared to the theoretical value (ca. 2.1 nm) of the PCN-M [200] plane, and the lattice is somewhat distorted. The crystal forms of different CPCN-Ms are similar to each other, as well as their textural properties. As shown in Fig. 2A, all the N_2 adsorption–desorption isotherms of CPCN-Ms feature typical IV type and exhibit a steep increase at low P/P_0 and an increase at $P/P_0 = 0.25$, suggesting microporosity and mesoporosity. The Brunauer–Emmett–Teller (BET) specific surface areas (S_{BET}) of CPCN-Fe, CPCN-Co, and CPCN-Ni are 2100, 2160, and 2130 $m^2\ g^{-1}$, respectively (Table S1). Note that S_{BET} of C_{60} is lower than 10 $m^2\ g^{-1}$ (Fig. S5), so the high S_{BET} values of CPCN-Ms are mainly from the host PCN-Ms. There are 2 types of pores for all CPCN-Ms, with sizes of 1.4 and 3.0 nm (Fig. 2A, inset), assigned to their triangular micro- and hexagonal meso-channels, respectively. The undifferentiated textural properties of CPCN-Ms ensure that their adsorption performances only depend on the intrinsic activity of the adsorption site, i.e., the metalloporphyrin ring, either at the ground state or at excited state.

Although the dispersed C_{60} ought to interact with the host PCN-M via van der Waals' forces [41], it can be proved that the interaction is intense. According to the thermogravimetric (TG) profiles, the weight loss at the temperature range higher than 650 °C can be observed for all CPCN-M samples, implying the intense interaction between C_{60} and PCN-M (Fig. S6). Moreover, the residual weights shown in the TG profiles conform to the theoretical ash contents of CPCN-Ms. The H-nuclear magnetic resonance (H-NMR) provides more convincing evidence. Taking the H-NMR of PCN-Co and CPCN-Co, for example (Fig. S7), owing to the shielding effect caused by C_{60}, the chemical shift δ of the porphin ring-*H* moves to higher magnetic field compared to that of PCN-Co, and correspondingly, the δ of both the proximal and the distal phenyl-*H* moves to lower magnetic field due to the deshielding effect. The intense interaction between C_{60} and the host PCN-M further influences the presentational valences of the porphyrin-coordinated metals. In Fig. 2B, obvious shake-up peaks can be observed in all x-ray photoelectron spectroscopy (XPS) spectra of CPCN-Ms, indicating that the experimentally introduced metals exist in the status of high valence, i.e., Fe(II), Co(II), or Ni(II), and the bivalence exhibits as the deconvolved peaks under their 2*p*3/2 bands correspondingly, such as those located at 708.7 and 709.9 eV for Fe(II), 781.7 eV for Co(II), and 852.3 eV for Ni(II), and other deconvolved peaks located at lower binding energies indicate the lower presentational valences for all CPCN-Ms. For example, the peaks located at

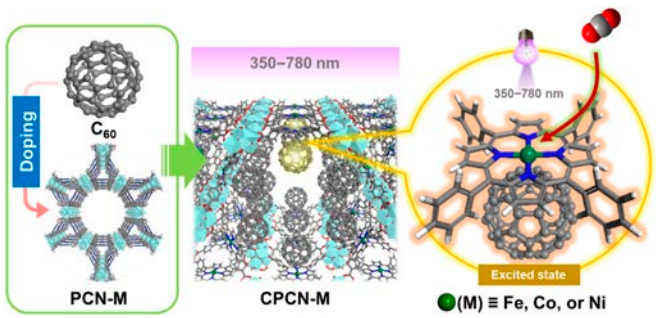


Fig. 1. The scheme of the composite CPCN-M construction and the nonderforming photo-responsiveness to enhance CO_2 adsorption capability over the metalloporphyrin-C_{60} site.

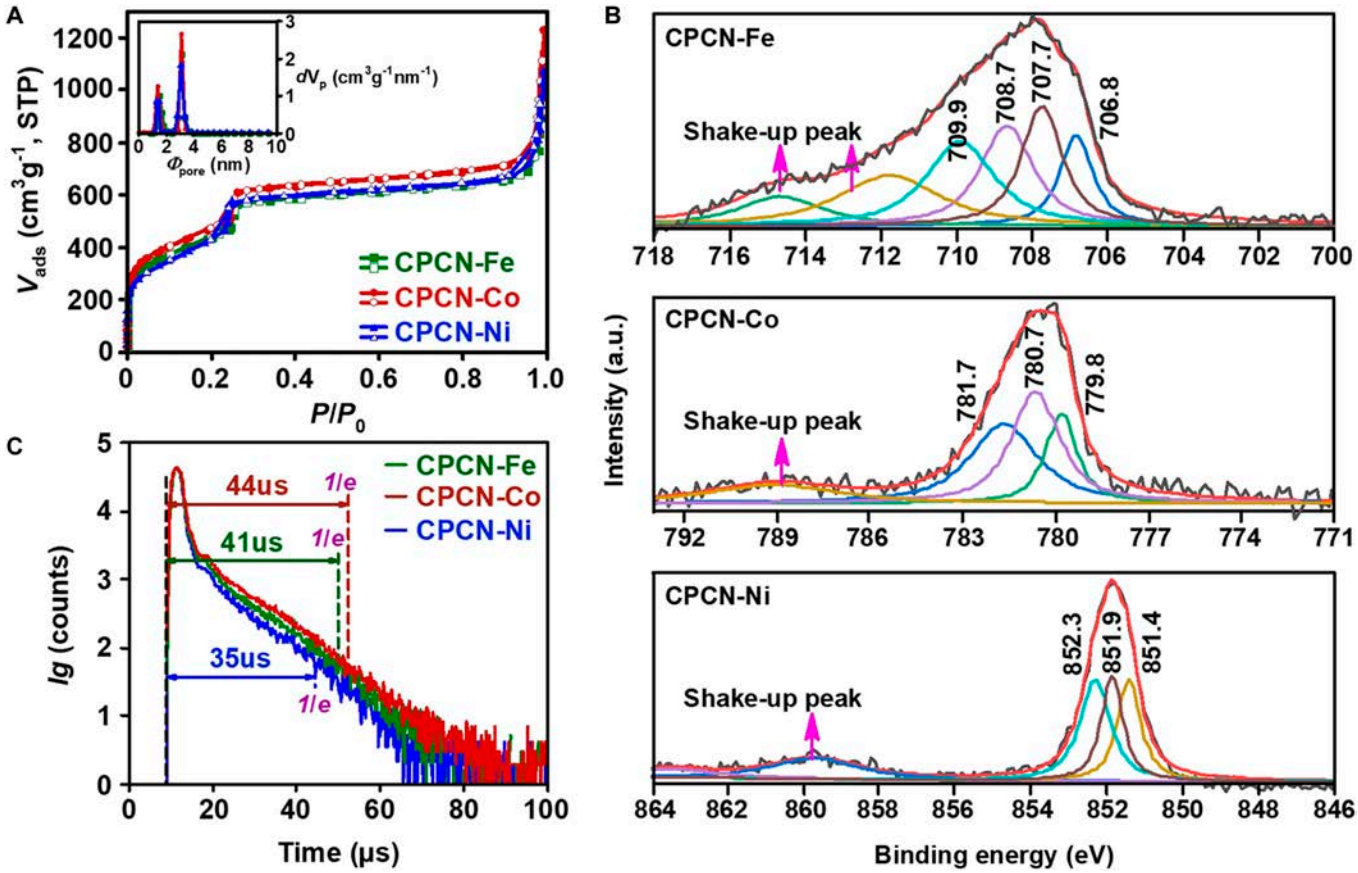


Fig. 2. Textural, optoelectronic, and phosphorescent properties of CPCN-Ms. (A) N_2 adsorption–desorption isotherms and pore size distribution (inset). (B) XPS deconvolution for the 2*p*3/2 band of the coordinated Fe, Co, and Ni. (C) Phosphor decay profiles at 750 nm, in which 1/*e* indicates the effective phosphorescence lifetime.

707.7 and 706.8 eV for CPCN-Fe should be caused by the porphyrin ring with large conjugate orbitals donating electrons and C_{60}-porphyrin ring cooperatively donating electrons to the coordinated Fe(II), respectively. The C_{60}-porphyrin ring cooperatively donating electrons is so intensive that the coordinated Fe(II) exhibits a tendency to be reduced to Fe(0) [42]. Such intense interaction between C_{60} and the porphyrin-coordinated metals is crucial for the photoinduced adsorption because the core metal is the decisive factor for CT and the formation of excited states.

Photoinduced adsorption

We have previously proved that although the metalloporphyrin and their derivatives can be excited to diverse orders with the UV or UV-Vis irradiation, de-excitation processes such as internal conversion, vibrational relaxation, and intersystem crossing must be rapid, and ultimately, the most stable low-order excited states will alter the EDD dominantly [24,25]. Without molecular deformation, the excitation-altered EDD substantially different from the EDD at the ground state must take an effective CT as a prerequisite, and the lifetime of the low-order excited state must be long enough to meet the timescale of molecular adsorption equilibrium (~10^{-6} s) [43,44]. With the 420-nm irradiation, the phosphorescent radiation related to the low-order excited states can be detected for all CPCN-Ms (Fig. S8). The corresponding phosphor decay profiles demonstrate that the effective lifetimes of the excited states for CPCN-Fe, CPCN-Co, and CPCN-Ni have reached 41, 44, and 35 μs, respectively (Fig. 2C). The lifetimes are durable enough to meet the molecular adsorption equilibrium. In contrast, although the phosphorescent radiation of C_{60} can also be detected, its effective lifetime is only 6 μs (Fig. S9). Moreover, in view of the poor textural property of C_{60} as mentioned above, it is safe to say that the isolated C_{60} aggregation, if any, would not perturb the investigation for the adsorption capabilities of the composite sorbents either at the ground state or at the excited state.

Owing to the intrinsic high S_{BET} value and microporosity, CPCN-Ms exhibit selective adsorption of CO_2 at ground states. As shown in Fig. 3A and Table S1, the adsorption capacities of CPCN-Fe, CPCN-Co, and CPCN-Ni in the darkness for CO_2 reach 2.08, 2.05, and 2.43 mmol g^{-1} at 0 °C and 1 bar, whereas those for N_2 are only 0.20, 0.14, and 0.13 mmol g^{-1}, respectively. The initial selectivity of CO_2 toward N_2 calculated with ideal adsorption solution theory can reach 124, 132, and 144, respectively (Fig. S10). As for the photoinduced adsorption experiments, the UV-Vis light with the wavelength of 350 to 780 nm was employed to sufficiently excite the sorbents because CPCN-Ms exhibited strong absorption at a wide UV-Vis range (Fig. S11). With the UV-Vis light, the CO_2 adsorption capacities of CPCN-Fe and CPCN-Co are elevated to 2.50 and 2.69 mmol g^{-1} at 0 °C and 1 bar, increased by 20% and 31%, respectively, while that of CPCN-Ni decreases to 1.99 mmol g^{-1} at 0 °C and 1 bar, with the loss rate of 18% instead (Fig. 3A, D, and E and Table S1). Compared to the CO_2 adsorption markedly changed

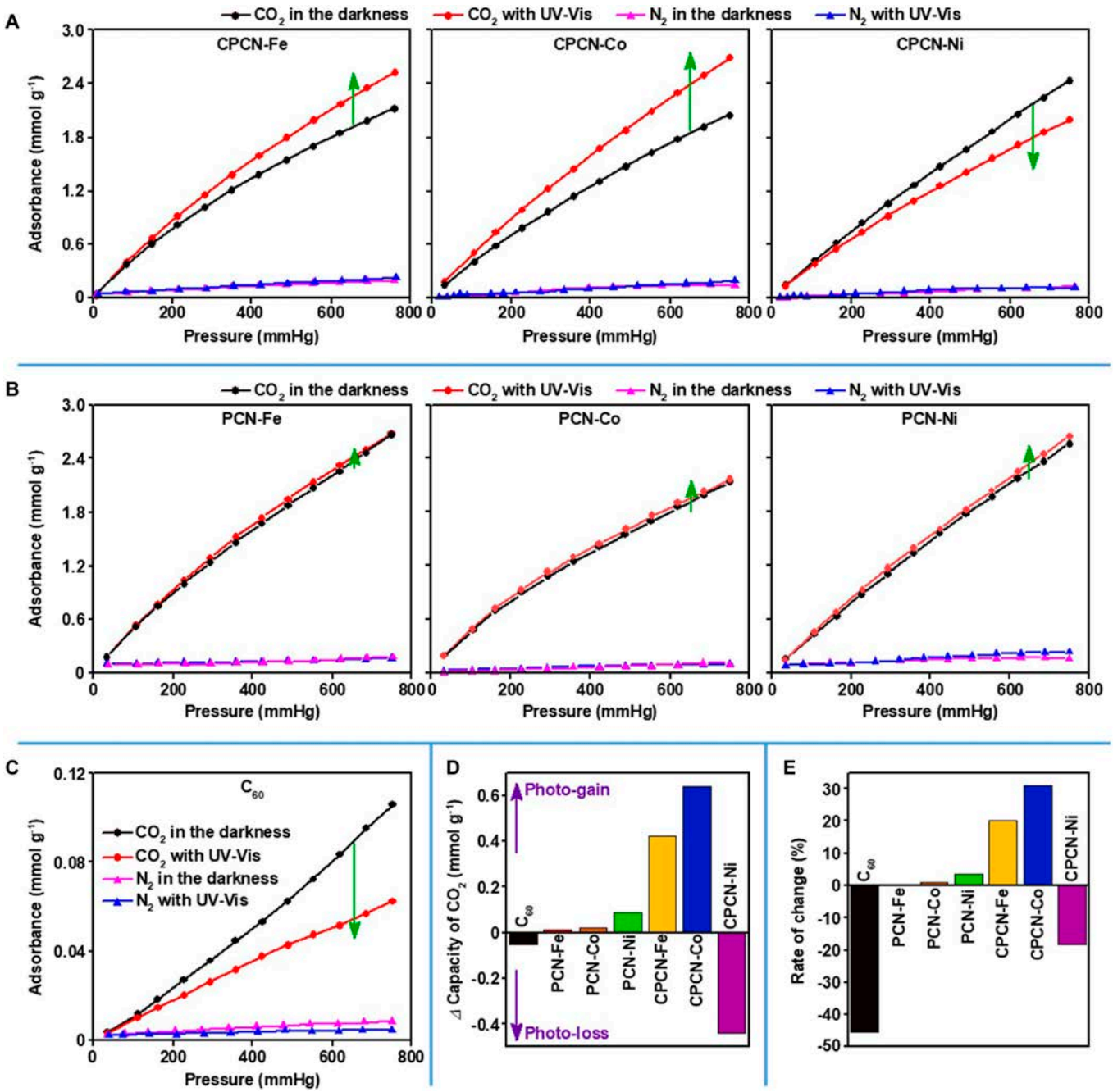


Fig. 3. The static adsorption isotherms of CO_2 and N_2 tested with UV-Vis irradiation and in the darkness over CPCN-Ms and PCN-Ms at 0 °C. (A) Static adsorption isotherms of CO_2 and N_2 over CPCN-Ms, in which the green arrows indicate the variation trend of the UV-Vis CO_2 adsorption isotherm with respect to that in the darkness. (B) Static adsorption isotherms of CO_2 and N_2 over PCN-Ms. (C) Static adsorption isotherms of CO_2 and N_2 over C_{60}. (D) Difference of the CO_2 uptake capacity at 1 bar with UV-Vis subtracting that in the darkness. (E) Rate of change for the photo-responsive CO_2 adsorption capacity at 1 bar.

by the UV-Vis irradiation, the UV-Vis influence on the N_2 adsorption over CPCN-Ms is imperceptible. The initial selectivity of CO_2 toward N_2 is thus changed to be 140, 164, and 108 for CPCN-Fe, CPCN-Co, and CPCN-Ni, respectively. In other words, the photo-gained adsorption capability of CO_2 can be achieved only over CPCN-Fe and CPCN-Co, and CPCN-Co exhibits more significant photo-responsiveness than CPCN-Fe.

As for the undoped materials, i.e., C_{60}, PCN-Fe, PCN-Co, and PCN-Ni, none of them exhibits obvious photo-responsiveness in terms of selective CO_2 adsorption (Fig. 3B and C). It is no wonder that the CO_2 uptake capacity of C_{60} at 0 °C and 1 bar is only 0.11 mmol g^{-1} in the darkness, and then decreases to 0.06 mmol g^{-1} with the UV-Vis irradiation, because its textual property is so poor as mentioned above, and as discussed below, the decrease of adsorption activity over C_{60} at the excited state must cause the CO_2 desorption. In contrast to the obvious photo-desorption of CO_2 over C_{60}, a noteworthy fact is that the CO_2 adsorption isotherms with the UV-Vis are almost coincided with those in the darkness for all PCN-Ms. This means that the photo-responsiveness of pristine PCN-Ms, if any, is too weak to

dramatically alter the CO_2 adsorption capability. These control experiments further verify the necessity of doping C_{60} in PCN-Ms to generate effective photo-responsiveness. Anyway, the doping amount of C_{60} should be optimized to balance the CO_2 adsorption capacity and the photo-responsiveness, and thus, the C_{60}/PCN-M mass ratio of 1:8 is proved to be appropriate (Fig. S12). The photo-responsiveness exhibited by CPCN-Ms ought to be strong enough, which is observable even at 25 °C (Fig. S13). Among the CPCN-M sorbents, the photoinduced CO_2 adsorption performance of CPCN-Co is competitive with other representative photo-responsive CO_2 sorbents during the past decade, especially when we consider that majority of the reported photo-responsive sorbents had to depend on deforming units, and the UV-Vis irradiation only caused the desorption over those sorbents (Table S2) [19,20,45–52]. Moreover, as the representative CPCN-M sorbent, CPCN-Co shows ideal ex situ reversibility, of which CO_2 adsorption capacity both at the ground state and with the UV-Vis irradiation can be well maintained even after five cycles (Fig. S14).

Mechanisms of photo-responsiveness

As mentioned above, owing to the C_{60} doping in the host PCN-Ms, all CPCN-Ms exhibit markedly nondeforming photo-responsiveness in terms of CO_2 adsorption capability, while the photo-responsiveness of CPCN-Fe and CPCN-Co exhibits as photo-gained CO_2 adsorption capability, and that of CPCN-Ni presents as the photo-loss on CO_2 uptake capacity. In contrast, none of the host PCN-Ms exhibits obvious photo-modulated effects on CO_2 adsorption compared to that without UV-Vis light. The underlying mechanisms are revealed through the calculations based on density functional theory (DFT) and time-dependent DFT (TDDFT). Here, tetraphenylporphyrin-M (TPP-M, M = Fe, Co, or Ni) is employed to simulate the corresponding adsorption site of PCN-M [24], and the C_{60}-TPP-M architecture (CTPP-M) is used to simulate that of CPCN-M, referring to Guldi's literature [41], of which C_{60} is located at the *c* axis of the porphin ring.

As for the non-bonded interaction like adsorption, we have proved that the nature of adsorption site can be indicated by the molecular surface electrostatic potential (ESP) [21,24,53]. The negative ESP area can be seen over TPP-Ms even at the ground state, which is mainly contributed by the conjugated electrons of porphin-*N* atoms, and the negative ESP interacts with the electron-deficient π_3^4 orbitals of the CO_2 molecule as strong van der Waals' force to capture it (Fig. S15). In contrast, the electron-full π_2^4 and σ_2^2 orbitals of N_2 molecule are much less prone to be induced by the negative ESP, which results in the high selectivity of CO_2 toward N_2 over the adsorption sites. Once TPP-M is excited, the original EDD at the ground state can be altered such that the maximal negative ESP is enhanced, which can induce and capture the CO_2 molecule more intensely. However, the enhancement of the negative ESP seems to be limited. For example, the maximal negative ESP over the TPP-Co is only changed from −30.0 meV at the ground state to −30.8 meV at the excited state. Such enhancement level might be just enough to offset the repulsion among the CO_2 molecules that are more gathered nearby the adsorption site due to the induction force enhanced with the negative ESP. Therefore, there is no significant difference between the CO_2 adsorption isotherms in the darkness and those with the UV-Vis light. As for CTPP-Ms, the excited states alter the EDD and the resultant ESP over the porphin ring powerfully due to the presence of C_{60}. As Fig. 4A exhibits, the maximal negative ESP values of CTPP-Fe and CTPP-Co are enhanced from −26.6 meV at the ground state to −31.3 meV at the excited state, and from −27.3 to −31.7 meV, respectively, whereas that of CTPP-Ni is weakened from −30.5 to −27.3 meV instead. Such obvious changes of ESP over the adsorption sites are enough to produce remarkable results on a macro level, and thus, the CO_2 adsorption isotherms over all CPCN-Ms can be markedly changed due to the UV-Vis irradiation. What is more, the different ESP changes over CTPP-Ms can well explain the experimental results of photo-gain for CPCN-Fe and CPCN-Co, but photo-loss for CPCN-Ni in terms of CO_2 adsorption capability.

The very different response modes of abovementioned adsorption sites to the UV-Vis excitation should be ascribed to the core metals and whether there is C_{60}. With the electron-hole distribution analysis for all the adsorption sites at excited states [54,55], both electrons and holes are mainly contributed by

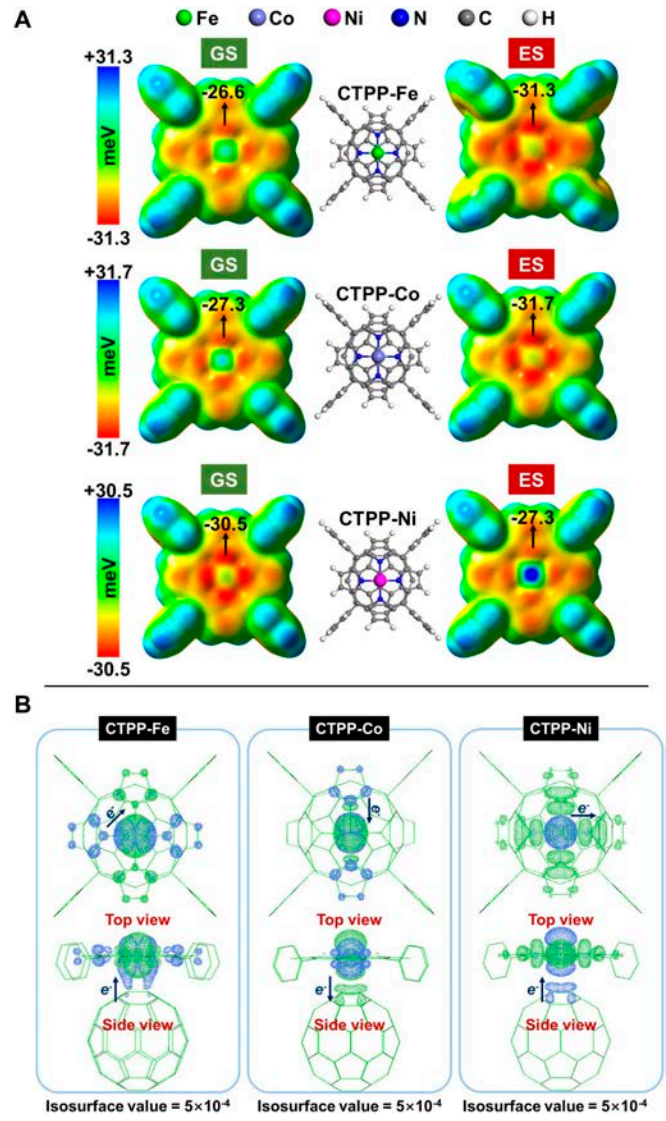


Fig. 4. The effect differences between the EDD at the excited state (ES) and that at the ground state (GS) for CTPP-M. (A) Molecular surface ESPs with the density isovalue = 1×10^{-3} at the ground and excited states. (B) The electron-hole distribution at the excited state (green area, electron distribution; blue area, hole distribution).

the core metals (Table S3). The DFT calculations prove that all TPP-Ms and CTPP-Ms are inner-orbital configurations, so the electronic configurations of the coordinated metals should be Fe-*d*[22110], Co-*d*[22210], and Ni-*d*[22220]. Because there are 2 and 1 unpaired *d*-electrons for Fe and Co, respectively, they are prone to accept the conjugated electrons from the porphin ring once excited. In contrast, Ni is prone to donate its electrons at the excited state. This is why the core metal can participate in the EDD alteration via excitation. As for TPP-Ms, the rearranged electrons are enriched over the core metals, resulting in an enhanced negative ESP (Fig. S16). However, both electrons and holes at excited states are mainly contributed by the core metals, and the electron hole is largely overlapped for TPP-Ms; in other words, the CT state over TPP-Ms is inapparent, so the enhancement of the negative ESP over TPP-Ms is limited.

As for CTPP-Ms, the *d* orbitals of the core metal are coupled with the 3-dimensional π-orbitals of C_{60} at the *c*-axis direction, which makes it possible to realize the CT state. As shown in Fig. 4B, the holes at excited states contributed by Fe and Ni are coupled with those by C_{60}, respectively, as well as the electrons at excited states contributed by Co. Although both the electrons and holes of the excited CTPP-Ms are still mainly contributed by the *d*-orbitals of the core metals, the symmetry of these areas is largely broken both at the *c*-axis direction and on the porphin ring, realizing the CT states. As a result, the variation of dipole moment μ with respect to the ground state for CTPP-M is much larger than that for the corresponding TPP-M due to CT at the *c*-axis direction, and the electron/hole delocalization indexes of the excited CTPP-M are all less than those of the excited TPP-M, indicating more delocalized electron/hole of CTPP-M than that of TPP-M due to CT on the porphin ring (Table S3). The excitation resultant CT states over CTPP-Ms are different from each other due to the different electron configurations of the core metals. The coordinated Fe ion of CTPP-Fe with 2 unpaired *d*-electrons can accept the electrons not only from the porphin ring but also from C_{60} at the excited state; meanwhile, the electrons from the porphin ring cannot be completely donated to the core Fe owing to the mismatched symmetry between orbitals, so the final result is that CT occurs not only between TPP-Fe and C_{60} but also between different areas on the porphin ring (Fig. 4B). The Co ion in CTPP-Co with one unpaired *d*-electron only causes electron donating from the porphin ring, and C_{60} also provides π-orbitals to jointly accept the electrons such that the electrons enriched at the *c*-axis direction are beneficial to the enhancement of negative ESP. The fully paired electrons of the Ni ion in CTPP-Ni once excited must be donated, and the hole coupled with C_{60} decentralizes the electrons on the porphin ring severely, so the negative ESP nearby the core Ni is weakened at the excited state. In addition, C_{60} itself cannot act as the CO_2 adsorption site, in view of its nearly neutral ESP at either the ground or excited state (Fig. S17), of which electron hole is almost completely overlapped in all directions on the C_{60} sphere (Fig. S18). In fact, the maximal negative ESP over C_{60} is even increased from −2.0 meV at the ground state to −0.2 meV at the excited state (Fig. S17), clearly indicating the decrease of its adsorption activity toward CO_2 at the excited state and explaining its reduced CO_2 adsorption capacity with the UV-Vis irradiation. Moreover, as a carbonaceous material, C_{60} may have the heat effect caused by the UV-Vis irradiation, with which the CO_2 capacity is reduced.

Discussion

The nondeforming photo-responsiveness of metalloporphyrin MOFs, i.e., PCN-222-Fe(II), PCN-222-Co(II), and PCN-222-Ni(II), is exploited in this study, with doping C_{60} in the host MOFs to construct the composite sorbents. In contrast to the current methodology to fabricate photo-responsive sorbents depending on the mechanical deformation of photochromic units, the nondeforming photo-responsiveness here is based on markedly changing the EDD over the metalloporphyrin adsorption sites via effective CT caused by excited states. Owing to the intense interaction of metalloporphyrin-C_{60} and their orbitals coupling, an effective CT path is built among the porphin ring, the coordinated metal, and C_{60}. The unpaired *d*-electrons make the porphin ring coordinated Fe(II) and Co(II) the electron-acceptors, over which the excited electrons can be enriched to enhance their adsorption activity, whereas the porphin ring coordinated Ni(II) with fully paired *d*-electrons acts as the electron-donor instead such that its excited electrons are decentralized to reduce the adsorption activity severely. In addition to the effective CT that modulates the EDD of adsorption sites, the low-order excited states of the composite sorbents possess long lifetimes, which meet the timescale of molecular adsorption equilibrium. As a result, the CO_2 adsorption capabilities of all the composite sorbents are obviously changed, and especially that of the Co(II)-coordinated one is significantly increased, with the UV-Vis irradiation.

Materials and Methods

Materials synthesis

All involved chemicals were commercially purchased and used as received. The materials are prepared according to the reported recipes with slight modifications [36–38]. To prepare the ligand of TCPP-M, the solution of 5,10,15,20-tetrakis (4-methoxycarbonylphenyl)porphyrin (TPPCOOMe, 1.0 mmol; purity > 95%; Yanshen, Jilin) and superfluous corresponding metal salt ($FeCl_2$, $CoCl_2$, or $NiCl_2$) in 100 ml of dimethyl formamide (DMF) was refluxed for 8 h. With H_2O added in the solution, the generated precipitate was filtered and then washed with H_2O sufficiently. The solid intermediate was dissolved in $CHCl_3$ and then sufficiently acidized with 1 M HCl. Washed with H_2O and dried with $MgSO_4$, the organic phase was evaporated to obtain the TCPP-M (M = Fe, Co, or Ni).

To prepare CPCN-M, C_{60}-fullerene (6 mg; purity > 99.9%; Macklin, Shanghai) was ultrasonically dissolved in toluene, followed by the addition of $ZrOCl_2{\cdot}8H_2O$ (120 mg), TCPP-M (31 mg), and benzoic acid (1.20 g) mixed in DMF (8.0 ml). The mixture was sealed in a stainless autoclave with Teflon inner liner and heated at 120 °C for 24 h. After cooling down to ambient temperature, the crystals were harvested by centrifugation and washed with toluene for wiping off the dissociative C_{60} particles, and then with DMF, tetrahydrofuran (THF), and CH_2Cl_2 successively, for further cleaning the unreacted ligands and exchanging the solvent molecules. After drying in vacuum, CPCN-M (M = Fe, Co, or Ni) was gotten eventually. The recipe for PCN-M preparation is similar to that of CPCN-M, but without the participation of C_{60}-toluene.

Characterization methods

The scanning electron microscope (SEM) images were scanned on a Nova NanoSEM 450 microscope. The HREM images were

observed on a JEM-2100F apparatus at an accelerating voltage of 200 kV. With Cu Kα at 40 kV and 40 mA, the XRPD patterns were tested with a Bruker D8 Advance diffractometer. With the KBr wafer, a Nicolet Nexus 470 spectrometer was used to record the FTIR spectra. The NMR spectroscopy was recorded with a Bruker AVANCE II 400M apparatus. The XPS was recorded on a Thermo Scientific Escalab 250Xi device with an Al Kα source. TG analyses in N_2 atmosphere were performed with a TG209F1 apparatus. The UV-Vis absorption spectra, the luminescence emission spectra, and the luminescence decay profiles of the samples were recorded at ambient temperature with an FLS1000 from Edinburgh Instruments. After degassing the materials at 100 °C for 4 h, the N_2 adsorption–desorption isotherms at 77 K were measured over a Micromeritics ASAP 2020 analyzer. S_{BET} was calculated at the P/P_0 range of 0.05 to 0.15. The total pore volumes were calculated at the relative pressure of 0.95, and the nonlocal DFT (NLDFT) was used to estimate the pore size distribution.

Static gas adsorption

Static adsorption experiments of CO_2 (purity > 99.999%) and N_2 (purity > 99.999%) over the sorbents were measured with the Micromeritics ASAP 2020 analyzer, respectively. The free space was determined using He (purity > 99.999%), with the assumption that He was not adsorbed. For pristine tests, the adsorption isotherms of CO_2 and N_2 were collected in a dark environment, with the sample cells immersed in an ice-water bath to keep the temperature at 0 °C or in a thermostatic water bath of 25 °C. For UV-Vis irradiation tests, a CEL-HXUV300 xenon lamp (optical power density: 2,000 mW cm^{-2}; Beijing China Education AuLight Technology Co. Ltd.) was used with a VisREF optical filter to generate the exciting light at the wavelength of 350 to 780 nm. The xenon lamp was placed 20 cm away from the sample cells to provide excitation light source, and other operation conditions were similar to the pristine ones.

Computational methods

The DFT and TDDFT calculations were performed by employing wB97XD functional implemented in Gaussian-16 package. The functional was proved to be robust for both DFT and TDDFT calculations [56,57]. With ultrafine numerical integration grids, self-consistent field procedures of full accuracy were performed with tight convergence and without any orbital symmetry constraints. The geometry relaxation was performed with the basis set of Def2-SVP. Four frontier excited states were involved in the TDDFT calculation with Tamm–Dancoff approximation in order to calculate the first excited state accurately.

Acknowledgments

We are grateful to the High-Performance Computing Center of Nanjing Tech University for supporting the computational resources.

Funding: We acknowledge financial support of this work by the National Natural Science Foundation of China (22178163, 22125804, and 22078155).

Author contributions: Conceptualization: S.-C.Q. and L.-B.S. Methodology: S.-C.Q., Z.-H.Y., and L.-B.S. Investigation: S.-C.Q., Z.S., Z.-H.Y., Y.-J.Z., J.-X.L., X.-Q.L., and L.-B.S. Writing—original draft: S.-C.Q. Writing—review and editing: S.-C.Q., L.-B.S., and X.-Q.L. Funding acquisition: L.-B.S., X.-Q.L., and S.-C.Q. Supervision: L.-B.S., S.-C.Q., and X.-Q.L.

Competing interests: The authors declare that they have no competing interests.

Data Availability

All data needed to evaluate the conclusions in the paper are present in the paper and/or the Supplementary Materials.

Supplementary Materials

Figs. S1 to S18
Tables S1 to S3

References

1. Pérez-Botella E, Valencia S, Rey F. Zeolites in adsorption processes: State of the art and future prospects. *Chem Rev*. 2022;122(24):17647–17695.
2. Wang YS, Zhang XJ, Ba YQ, Li TY, Hao GP, Lu AH. Recent advances in carbon-based adsorbents for adsorptive separation of light hydrocarbons. *Research*. 2022;2022:9780864.
3. Halder A, Klein RA, Shulda S, McCarver GA, Parilla PA, Furukawa H, Brown CM, McGuirk CM. Multivariate flexible framework with high usable hydrogen capacity in a reduced pressure swing process. *J Am Chem Soc*. 2023;145(14):8033–8042.
4. Gong W, Xie Y, Wang XJ, Kirlikovali KO, Idrees KB, Sha FR, Xie HM, Liu Y, Chen BL, Cui Y, et al. Programmed polarizability engineering in a cyclen-based cubic Zr(IV) metal-organic framework to boost Xe/Kr separation. *J Am Chem Soc*. 2023;145(4):2679–2689.
5. Wang QJ, Hu JB, Yang LF, Zhang ZQ, Ke T, Cui XL, Xing HB. One-step removal of alkynes and propadiene from cracking gases using a multi-functional molecular separator. *Nat Commun*. 2022;13(1):2955.
6. Li YJ, Cui JY, Wang QJ, Yang LF, Chen LY, Xing HB, Cui XL. Responsive shape recognition of styrene over ethylbenzene with excellent selectivity and capacity in a hybrid porous material. *Chem Eng J*. 2023;453(2):Article 139756.
7. Guo ZD, Cui JY, Li YJ, Zhang PX, Yang LF, Chen LY, Wang J, Cui XL, Xing HB. Responsive porous material for discrimination and selective capture of low-concentration SO_2. *Ind Eng Chem Res*. 2022;61(17):5936–5941.
8. Li HQ, Hill MR. Low-energy CO_2 release from metal-organic frameworks triggered by external stimuli. *Acc Chem Res*. 2017;50(4):778–786.
9. Castellanos S, Kapteijn F, Gascon J. Photoswitchable metal organic frameworks: Turn on the lights and close the windows. *CrystEngComm*. 2016;18(22):4006–4012.
10. Qiao YT, Bailey JJ, Huang Q, Ke XB, Wu CF. Potential photo-switching sorbents for CO_2 capture—A review. *Renew Sust Energ Rev*. 2022;158:Article 112079.
11. Lyndon R, Konstas K, Evans RA, Keddie DJ, Hill MR, Ladewig BP. Tunable photodynamic switching of DArE@PAF-1 for carbon capture. *Adv Funct Mater*. 2015;25(28):4405–4411.
12. He JP, Aggarwal K, Katyal N, He SC, Chiang E, Dunning SG, Reynolds JE, Steiner A, Henkelman G, Que EL, et al. Reversible solid-state isomerism of azobenzene-loaded large-pore Isoreticular Mg-CUK-1. *J Am Chem Soc*. 2020;142(14):6467–6471.

13. Li ZQ, Wang GN, Ye YX, Li B, Li HR, Chen BL. Loading photochromic molecules into a luminescent metal-organic framework for information anticounterfeiting. *Angew Chem Int Ed*. 2019;58(50):18025–18031.
14. Zhao YQ, Li Z, Ma JT, Jia Q. Design of a spiropyran-based smart adsorbent with dual response: Focusing on highly efficient enrichment of phosphopeptides. *ACS Appl Mater Interfaces*. 2021;13(47):55806–55814.
15. Krause S, Evans JD, Bon V, Crespi S, Danowski W, Browne WR, Ehrling S, Walenszus F, Wallacher D, Grimm N, et al. Cooperative light-induced breathing of soft porous crystals via azobenzene buckling. *Nat Commun*. 2022;13(1):1951.
16. Liu JT, Wang SF, Huang TF, Manchanda P, Abou-Hamad E, Nunes SP. Smart covalent organic networks (CONs) with "on-off-on" light-switchable pores for molecular separation. *Sci Adv*. 2020;6(34):eabb3188.
17. Zhu J, Tan P, Yang PP, Liu XQ, Jiang Y, Sun LB. Smart adsorbents with reversible photo-regulated molecular switches for selective adsorption and efficient regeneration. *Chem Commun*. 2016;52(77):11531–11534.
18. Wang ZB, Knebel A, Grosjean S, Wagner D, Bräse S, Woll C, Caro J, Heinke L. Tunable molecular separation by nanoporous membranes. *Nat Commun*. 2016;7:13872.
19. Park J, Yuan DQ, Pham KT, Li JR, Yakovenko A, Zhou HC. Reversible alteration of CO_2 adsorption upon photochemical or thermal treatment in a metal-organic framework. *J Am Chem Soc*. 2012;134(1):99–102.
20. Gong LL, Feng XF, Luo F. Novel azo-metal-organic framework showing a 10-connected bct net, breathing behavior, and unique photoswitching behavior toward CO_2. *Inorg Chem*. 2015;54(24):11587–11589.
21. Jiang Y, Tan P, Qi SC, Liu XQ, Yan JH, Fan F, Sun LB. Metal-organic frameworks with target-specific active sites switched by photoresponsive motifs: Efficient adsorbents for tailorable CO_2 capture. *Angew Chem Int Ed*. 2019;58(20):6600–6604.
22. Wang ZB, Grosjean S, Bräse S, Heinke L. Photoswitchable adsorption in metal-organic frameworks based on polar guest-host interactions. *ChemPhysChem*. 2015;16(18):3779–3783.
23. Moreno JR, Carleo G, Georges A. Deep learning the Hohenberg-Kohn maps of density functional theory. *Phys Rev Lett*. 2020;125(7):Article 076402.
24. Qi SC, Yu YF, Yang ZH, Liu XY, Lu XJ, Liu XQ, Sun LB. Active sites modulation with Runge-Gross theorem: CO_2 capture by porphyrinic metal-organic frameworks at excited states. *AICHE J*. 2023;69(5):Article e17994.
25. Qi SC, Liu YL, Lu XJ, Zhao YJ, Li JX, Liu XQ, Sun LB. Enhanced CO adsorption by modulating the electron density distribution of graphite-copper porphyrin sorbents with light. *Angew Chem Int Ed*. 2023;135(27):Article e202304367.
26. Zhang LX, Qi MY, Tang ZR, Xu YJ. Heterostructure-engineered semiconductor quantum dots toward photocatalyzed-redox cooperative coupling reaction. *Research*. 2023;6:0073.
27. Song JN, Zhang M, Hao TY, Yan J, Zhu L, Zhou GQ, Zeng R, Zhong WK, Xu JQ, Zhou ZC, et al. Design rules of the mixing phase and impacts on device performance in high-efficiency organic photovoltaics. *Research*. 2022;2022:9817267.
28. Wang FF, Chang Q, Yun YK, Liu SZ, Liu Y, Wang JA, Fang YY, Cheng ZC, Feng SL, Yang LF, et al. Hole-transporting low-dimensional perovskite for enhancing photovoltaic performance. *Research*. 2021;2021:9797053.
29. Yamada M, Ohkubo K, Shionoya M, Fukuzumi S. Photoinduced electron transfer in a charge-transfer complex formed between corannulene and $Li^+@C_{60}$ by concave-convex π-π interactions. *J Am Chem Soc*. 2014;136(38):13240–13248.
30. Zarrabi N, Seetharaman S, Chaudhuri S, Holzer N, Batista VS, van der Est A, D'Souza F, Poddutoori PK. Decelerating charge recombination using fluorinated porphyrins in *N*,*N*-bis(3,4,5-trimethoxyphenyl)aniline-aluminum(III) porphyrin-fullerene reaction center models. *J Am Chem Soc*. 2020;142(22):10008–10024.
31. Qi SC, Liu Y, Peng AZ, Xue DM, Liu X, Liu XQ, Sun LB. Fabrication of porous carbons from mesitylene for highly efficient CO_2 capture: A rational choice improving the carbon loop. *Chem Eng J*. 2019;361:945–952.
32. Qi SC, Yu GX, Xue DM, Liu X, Liu XQ, Sun LB. Rigid supramolecular structures based on flexible covalent bonds: A fabrication mechanism of porous organic polymers and their CO_2 capture properties. *Chem Eng J*. 2020;385:Article 123978.
33. Sanz-Pérez ES, Murdock CR, Didas SA, Jones CW. Direct capture of CO_2 from ambient air. *Chem Rev*. 2016;116(19):11840–11876.
34. Zhu XC, Xie WW, Wu JY, Miao YH, Xiang CJ, Chen CP, Ge BY, Gan ZZ, Yang F, Zhang M, et al. Recent advances in direct air capture by adsorption. *Chem Soc Rev*. 2022;51(15):6574–6651.
35. Xu XY, Kentish SE, Martin GJO. Direct air capture of CO_2 by microalgae with buoyant beads encapsulating carbonic anhydrase. *ACS Sustain Chem Eng*. 2021;9(29):9698–9706.
36. Feng DW, Gu ZY, Li JR, Jiang HL, Wei ZW, Zhou HC. Zirconium-metalloporphyrin PCN-222: Mesoporous metal-organic frameworks with ultrahigh stability as biomimetic catalysts. *Angew Chem Int Ed*. 2012;51(41):10307–10310.
37. Feng DW, Chung WC, Wei ZW, Gu ZY, Jiang HL, Chen YP, Darensbourg DJ, Zhou HC. Construction of ultrastable porphyrin Zr metal-organic frameworks through linker elimination. *J Am Chem Soc*. 2013;135(45):17105–17110.
38. Zheng DY, Chen EX, Ye CR, Huang XC. High-efficiency photo-oxidation of thioethers over C_{60}@PCN-222 under air. *J Mater Chem A*. 2019;7(38):22084–22091.
39. Oku T, Kubota H, Ohgami T, Suganuma K. Possible detection of doping atoms in C_{60} solid clusters by high-resolution electron microscopy. *Carbon*. 1999;37(8):1299–1309.
40. Cid A, Moldes ÓA, Diniz MS, Rodríguez-González B, Mejuto JC. Redispersion and self-assembly of C_{60} fullerene in water and toluene. *ACS Omega*. 2017;2(5):2368–2373.
41. Guldi DM. Fullerene-porphyrin architectures; photosynthetic antenna and reaction center models. *Chem Soc Rev*. 2002;31(1):22–36.
42. Powell CJ. Recommended auger parameters for 42 elemental solids. *J Electron Spectrosc Relat Phenom*. 2012;185(1-2):1–3.
43. Wang RL, Wang XY, Zuo ZJ, Ni SJ, Dai J, Wang DW. Adsorption equilibrium and mechanism and of water molecule on the surfaces of molybdenite (MoS_2) based on kinetic Monte-Carlo method. *Molecules*. 2022;27(24):8710.
44. Ren FY, Waite SW, Harris JM. Temperature-jump investigation of adsorption/desorption kinetics at methylated silica/solution interfaces. *Anal Chem*. 1995;67(19):3441–3447.
45. Lyndon R, Konstas K, Ladewig BP, Southon PD, Kepert CJ, Hill MR. Dynamic photo-switching in metal-organic frameworks as a route to low-energy carbon dioxide capture and release. *Angew Chem Int Ed*. 2013;52(13):3695–3698.

46. Huang RH, Hill MR, Babarao R, Medhekar NV. CO_2 adsorption in azobenzene functionalized stimuli responsive metal-organic frameworks. *J Phys Chem C*. 2016;120(30):16658–16667.
47. Prasetya N, Ladewig BP. New Azo-DMOF-1 MOF as a photoresponsive low-energy CO_2 adsorbent and its exceptional CO_2/N_2 separation performance in mixed matrix membranes. *ACS Appl Mater Interfaces*. 2018;10(40):34291–34301.
48. Cheng L, Jiang Y, Qi SC, Liu W, Shan SF, Tan P, Liu XQ, Sun LB. Controllable adsorption of CO_2 on smart adsorbents: An interplay between amines and photoresponsive molecules. *Chem Mater*. 2018;30(10):3429–3437.
49. Li SY, Prasetya N, Ladewig BP. Investigation of Azo-COP-2 as a photoresponsive low-energy CO_2 adsorbent and porous filler in mixed matrix membranes for CO_2/N_2 separation. *Ind Eng Chem Res*. 2019;58(23):9959–9969.
50. Jiang Y, Shi XC, Tan P, Qi SC, Gu C, Yang T, Peng SS, Liu XQ, Sun LB. Controllable CO_2 capture in metal-organic frameworks: Making targeted active sites respond to light. *Ind Eng Chem Res*. 2020;59(50):21894–21900.
51. Tashiro K, Otori M, Satokawa S. Photo-induced mode change for CO_2 capture/release on spiropyran in a polar-gradient environment. *Chem Commun*. 2023;59(29):4304–4307.
52. Liu AT, Mollart C, Trewin A, Fan XF, Lau CH. Photo-modulating CO_2 uptake of hypercross-linked polymers upcycled from polystyrene waste. *ChemSusChem*. 2023;16:Article e202300019.
53. Qi SC, Wu JK, Lu J, Yu GX, Zhu RR, Liu Y, Liu XQ, Sun LB. Underlying mechanism of CO_2 adsorption onto conjugated azacyclo-copolymers: N-doped adsorbents capture CO_2 chiefly through acid-base interaction? *J Mater Chem A*. 2019;7(30):17842–17853.
54. Lu T, Chen FW. Multiwfn: A multifunctional wavefunction analyzer. *J Comput Chem*. 2012;33(5):580–592.
55. Liu ZY, Lu T, Chen QX. An sp-hybridized all-carboatomic ring, cyclo[18]carbon: Electronic structure, electronic spectrum, and optical nonlinearity. *Carbon*. 2020;165: 461–467.
56. Fei ETL, Biswas J, Datta B, Kumar D. Computational studies of diindole-based molecules for organic bulk heterojunction solar devices using DFT and TD-DFT calculations. *Struct Chem*. 2021;32(5):1973–1984.
57. De Simone BC, Marino T, Russo N. TDDFT investigation on methylviologen, 3,7-diazabenzophosphole, and helical helquat electrochromic systems. *Theor Chem Accounts*. 2016;135(5):118.